International Journal of Heat and Mass Transfer 81 (2015) 721–736

Contents lists available at ScienceDirect

International Journal of Heat and Mass Transfer

journal homepage: www.elsevier.com/locate/ijhmt

Flow boiling in microgravity: Part 2 – Critical heat flux interfacial behavior, experimental data, and model

Christopher Konishi [a], Hyoungsoon Lee [a], Issam Mudawar [a,*], Mohammad M. Hasan [b], Henry K. Nahra [b], Nancy R. Hall [b], James D. Wagner [b], Rochelle L. May [b], Jeffrey R. Mackey [c]

[a] Purdue University Boiling and Two-Phase Flow Laboratory (PU-BTPFL), School of Mechanical Engineering, 585 Purdue Mall, West Lafayette, IN 47907, USA
[b] NASA Glenn Research Center, 21000 Brookpark Road, Cleveland, OH 44135, USA
[c] Vantage Partners, LLC, 3000 Aerospace Parkway, Brook Park, OH 44142, USA

ARTICLE INFO

Article history:
Received 9 August 2014
Received in revised form 21 October 2014
Accepted 21 October 2014
Available online 21 November 2014

Keywords:
Microgravity
Flow boiling
Interfacial behavior
Critical heat flux

ABSTRACT

This study is the second part of a two-part investigation of flow boiling critical heat flux (CHF) in microgravity, which is simulated in parabolic flight experiments. Using FC-72 as working fluid, flow boiling experiments are conducted in a rectangular channel fitted with two opposite heated walls, allowing either one or both heated walls to be activated during a test. While the first part explored flow boiling conditions leading to CHF, this part addresses events just before CHF, during the CHF transient, and immediately following CHF. For both single-sided and double-sided heating, interfacial behavior just before CHF is characterized by dominant wavy vapor layers covering the heated walls, where liquid is able to access the walls only in wetting fronts corresponding to the wave troughs. CHF is associated with successive lift-off of wetting fronts from the walls, consistent with the Interfacial Lift-off Model, which has been validated extensively in past studies using single-sided heating in both μg_e and $1 - g_e$. It is shown this model predicts μg_e double-sided flow boiling CHF with excellent accuracy. Additionally, the model points to convergence of CHF values for μg_e and $1 - g_e$ for inlet velocities greater than about 1 m/s. Therefore, by maintaining velocities above this threshold allows designers of space systems to achieve inertia-dominated performance as well as to adopt prior data and correlations developed from terrestrial studies.

1. Introduction

1.1. Implementation of flow boiling and condensation in future space missions

For decades, thermal management onboard manned space vehicles has been tackled by conventional single-phase systems that absorb the heat by raising the sensible heat of an appropriate coolant, and reject it to deep space via a space radiator. This type of system has been used successfully on all of NASA's Space Shuttles. However, there is now specific interest in long duration space missions, especially the manned mission to Mars, which are expected to pose many technological challenges, especially the need to greatly increase energy efficiency and reduce both the weight and volume of the entire systems [1,2], including the Thermal Control System (TCS) responsible for maintaining the temperature and humidity of the operating environment. These benefits will be realized by shifting from present single-phase liquid thermal management to two-phase counterpart. By capitalizing on both sensible and latent heat of the coolant instead of sensible heat alone, two-phase systems can yield orders of magnitude enhancement in flow boiling and condensation heat transfer coefficients while significantly reducing the temperature of the heat dissipating device compared to single-phase systems.

Two-phase thermal management systems utilizing flow boiling and condensation have attracted significant interest in recent years in many applications demanding efficient heat removal from high-power-density devices, including computer data centers, hybrid vehicle power electronics and avionics [3,4]. The effectiveness of these systems has been demonstrated using a variety of boiling configurations, including pool [5,6], macro-channel flow [7,8], micro-channel flow [9], jet [10,11], and spray [12–14], as well as hybrid schemes combining the merits of two or more boiling configurations [15,16].

However, the feasibility of a particular boiling configuration in a space vehicle's TCS is dependent on a number of considerations, which include, aside from reduced weight and volume, low pumping power and the ability to manage phase separation in a closed

* Corresponding author. Tel.: +1 (765) 494 5705; fax: +1 (765) 494 0539.
E-mail address: mudawar@ecn.purdue.edu (I. Mudawar).
URL: https://engineering.purdue.edu/BTPFL (I. Mudawar).

http://dx.doi.org/10.1016/j.ijheatmasstransfer.2014.10.052
0017-9310/

Nomenclature

A	cross-sectional area of flow channel
$A_{w,w}$	area of wetting front
b	ratio of wetting front length to wavelength
$C_{f,i}$	interfacial friction coefficient
c	wave speed
c_i	imaginary component of wave speed
c_p	specific heat at constant pressure
c_r	real component of wave speed
D	hydraulic diameter
f	friction factor
G	mass velocity
g	gravity
g_e	Earth's gravitational acceleration
H	height of flow channel's cross-section
h_{fg}	latent heat of vaporization
k	wave number
L	length
L_d	development length of flow channel
L_e	exit length of channel
L_h	heated length of channel
MAE	mean absolute error
$\dot{m}$	mass flow rate
N	number of data points
p	pressure
P_i	interfacial perimeter
P_w	wall friction perimeter
q''_m	critical heat flux
q''_w	wall heat flux
$q''_{w,w}$	wetting front heat flux
Re	Reynolds number
T	temperature
t	time
T_{in}	inlet temperature
T_{sat}	saturation temperature
T_w	wall temperature
$\Delta T_{sub,in}$	inlet subcooling, $T_{sat} - T_{in}$
U	mean inlet liquid velocity; mean axial velocity
u_i	interfacial velocity
W	width of flow channel's cross-section
x	flow quality
y	coordinate normal to heated wall
z	axial distance
z_o	axial location where vapor layer velocity just exceeds liquid layer velocity
z^*	axial location for determining vapor layer thickness and critical wavelength in Interfacial Lift-off Model

Greek symbols

α	vapor void fraction
Γ_{fg}	evaporation rate per unit distance
δ	mean vapor layer thickness
η	interfacial perturbation
η_0	amplitude of interfacial perturbation
θ	flow orientation angle
λ	wavelength
λ_c	critical wavelength
μ	dynamic viscosity
ρ	density
ρ''	modified density
σ	surface tension
τ_i	interfacial shear stress
τ_w	wall shear stress

Subscripts

est	estimated
exp	experimental (measured)
f	saturated liquid; bulk liquid
g	saturated vapor
i	interfacial
in	inlet to heated portion of flow channel
k	phase k, $k = g$ or f
m	maximum (CHF); heated wall identifier ($m = 1$ for H_1, $m = 2$ for H_2)
n	normal to heated wall; thermocouple location along heated wall
o	outlet from heated portion of flow channel
pred	predicted
sat	saturation
sub	subcooling
w	wall; wetting front

TCS loop in microgravity. These considerations preclude spray and jet configurations as viable options. Pool boiling is also very problematic in microgravity because it has been shown to produce massive bubbles upon the heated wall that significantly decrease critical heat flux (CHF) compared to terrestrial pool boiling [17]. These reasons are why flow boiling, using macro-channels or micro-channels, is presently the configuration most favored for the space vehicle's TCS. Even in microgravity, flow inertia in flow boiling serves to maintain high CHF by flushing bubbles away from the heated wall before they coalesce into insulating blankets, and by maintaining liquid replenishment of the heated wall. This is especially important to heat-flux-controlled devices, such as avionics, where CHF occurrence can lead to physical meltdown, burnout, or catastrophic damage to the heat-dissipating surface and surrounding components.

But, while the merits of flow boiling are well acknowledged, design engineers lack the data and technical knowhow to assess the influence of reduced gravity on flow boiling CHF. Flow boiling is obviously highly influenced by the large density differences between liquid and vapor, which, in the terrestrial environment, yield an appreciable buoyancy force that helps dictate both flow behavior and heat transfer effectiveness. However, in reduced gravity, especially microgravity, body force is much weaker, meaning flow behavior is dictated more by other forces such as inertia and surface tension. This brings into question the applicability of terrestrial flow boiling data, models and correlations to reduced gravity. To correct this knowledge gap, flow boiling experiments must be performed in reduced gravity, aided by flow visualization methods, to facilitate a comprehensive fundamental understanding of interfacial behavior and the roles of dominant forces.

1.2. Postulated mechanisms for flow boiling CHF in Earth gravity

CHF is arguably the most important design parameter for flow boiling systems involving thermal management of heat-flux-controlled surfaces. Most attempts to model flow boiling CHF concern vertical upflow in Earth gravity, which is the orientation that provides both stable two-phase flow and favorable CHF values. The most crucial component of these models is predicting the physical mechanism responsible for initiating – triggering – flow boiling

CHF. Four popular mechanisms have been proposed: *Boundary Layer Separation*, *Bubble Crowding*, *Sublayer Dryout*, and *Interfacial Lift-off*. The Boundary Layer Separation Model [18,19] utilizes analogy between wall gas injection – transpiration – into a single-phase liquid boundary layer and wall vapor effusion in flow boiling. As injection velocity into a liquid boundary layer is increased to a critical value, the velocity gradient near the wall becomes vanishingly small, causing the boundary layer to separate from the wall. By analogy, CHF is assumed to occur when the rate of vapor effusion perpendicular to the wall in flow boiling reaches a threshold that triggers sharp reduction in velocity gradient of liquid flow adjacent to the heated wall, which causes separation of the liquid boundary layer and extinguishes liquid replenishment of the heated wall. The Bubble Crowding Model [20,21] is based on an entirely different depiction of the flow adjacent to the heated wall. Here, severe boiling causes accumulation of oblong bubbles near the wall, and CHF is postulated to occur when the bubbly layer becomes too crowded with bubbles to permit turbulent fluctuations in the core liquid to supply adequate liquid to the wall. The Sublayer Dryout Model [22] depicts the formation of oblong vapor blankets along the heated wall, trapping thin liquid sublayers, which are sustained by liquid replenishment from the bulk liquid. CHF is postulated to occur when the heat supplied from the wall exceeds the enthalpy of bulk liquid replenishing the sublayer. The Interfacial Lift-off Model [23,24] is based on the observation that vigorous boiling generates vapor patches along the heated wall, which coalesce into a fairly continuous wavy vapor layer. Cooling of the wall is sustained mostly by vigorous boiling in "wetting fronts," which correspond to the wavy layer troughs making contact with the wall. CHF is postulated to occur when the momentum of vapor produced in the wetting fronts normal to the heated wall becomes sufficiently intense to lift the interface away from the wall, extinguishing liquid replenishment of the wall.

Given that these flow boiling models have been developed mostly for vertical upflow in Earth gravity, the validity of the trigger mechanisms proposed in the development of these models to reduced gravity will require performing systematic flow boiling experiments aided by flow visualization methods to capture dominant interfacial behavior.

1.3. Pressure drop in microgravity flow boiling

Although research on boiling heat transfer in reduced gravity spans over half a century, the majority of published literature concerns pool boiling and adiabatic two-phase flow patterns. With only a few studies addressing flow boiling in reduced gravity, especially microgravity (μg_e), there is now a critical shortage of literature specifically related to fluid flow, pressure drop, nucleate boiling heat transfer and CHF in μg_e flow boiling.

A few investigators explored pressure drop in μg_e flow boiling. Luciani et al. [25,26] performed parabolic flight experiments to investigate flow boiling of HFE-7100 in rectangular channels (6.0×0.254, 6.0×0.454, $6.0 \times 0.654\ mm^2$ by 50-mm long). The μg_e and hypergravity ($1.8 - g_e$) pressure drop data from these experiments were also analyzed by Brutin et al. [27] and compared to terrestrial ($1 - g_e$) data. They found the two-phase frictional pressure drop to increase with increasing gravity, which they attributed to an observed decrease in void fraction increasing the portion of the channel's cross-sectional area dedicated to liquid flow. Interestingly, this trend contradicts experimental findings from adiabatic two-phase flow studies [28–30], which found the two-phase frictional pressure drop to increase in μg_e, especially at low flow rates. Misawa [31] performed both drop tower and parabolic flight experiments to investigate flow boiling of R-113 in μg_e. They used a square channel ($5 \times 5\ mm^2$ by 500-mm long) equipped with a heating film, and two electrically heated coiled tubes (4 and 12.8-mm diameter, 500 and 480-mm long). The wall shear stress in μg_e was found to be 1.18 times larger than in $1 - g_e$, which they attributed to larger bubbles in the low-quality region in μg_e.

1.4. Flow boiling CHF in microgravity

Published μg_e pool boiling studies provide ample evidence that CHF is reduced significantly in μg_e compared to $1 - g_e$ [32–34]. Absent a body force to remove vapor bubbles from the heated wall, the decrease in CHF is attributed mostly to bubble coalescence into an unusually large bubble encompassing the entire heated wall. As pointed out earlier, flow boiling provides a practical and effective means to preventing the formation of massive bubbles by relying on liquid inertia to flush discrete bubbles away from the heated wall and sustain liquid replenishment of the wall. But, while the effectiveness of flow boiling might seem quite obvious, supporting experimental evidence is very limited, given that very few studies have been dedicated exclusively to flow boiling CHF in μg_e.

Ohta [35] obtained limited flow boiling CHF data in μg_e at high inlet quality, but noted that they could not measure CHF accurately in the absence of local wall temperature measurements along the heated wall. Ma and Chung [36] investigated subcooled flow boiling of FC-72 across a heated 0.254-mm platinum wire in a 2.1-s drop tower. They measured a substantial shift in the μg_e boiling curve to lower heat fluxes compared to $1 - g_e$, indicating significant reduction in heat transfer effectiveness. CHF was also significantly lower in μg_e. However, differences in both heat transfer rate and CHF between μg_e and $1 - g_e$ decreased with increasing flow rate.

Zhang et al. conducted subcooled flow boiling CHF experiments with FC-72 both at $1 - g_e$ [37–41] and in reduced gravity [42,43]. They employed a $2.5 \times 5.0\ mm^2$ rectangular flow channel that was fitted along one of the 2.5-mm sides with a 101.6-mm long heated copper wall. In their terrestrial experiments, the flow channel was tilted to different orientations relative to Earth gravity. Using one heated wall allowed them to isolate the component of Earth gravity perpendicular to the heated wall. The flight experiments were used to measure CHF in μg_e, Lunar gravity ($0.17 - g_e$) and Martian gravity ($0.38 - g_e$).

Fig. 1(a) and (b) shows CHF behavior for different flow orientations at $1 - g_e$ [37]. The orientations $\theta = 0°$ and 180° corresponding to horizontal flow with the heated wall facing upwards and downwards, respectively, and $\theta = 90°$ and 270° corresponding to vertical upflow and downflow, respectively. Fig. 1(a) shows interfacial behavior at CHF- (just preceding CHF) for slightly subcooled flow and $U = 0.1$ m/s. At this low velocity, orientation has an appreciable influence on CHF because of low flow inertia, evidenced by large differences in CHF magnitude among the four orientations at $U = 0.1$ m/s. Fig. 1(a) shows four distinct CHF regimes: (i) Pool-Boiling Regime for $\theta = 0°$, (ii) Wavy Vapor Layer Regime for $\theta = 90°$, (iii) Stratification Regime for $\theta = 180°$, and (iv) Vapor Stagnation Regime for $\theta = 270°$. In the Pool Boiling Regime ($\theta = 0°$), bubbles coalesce along the heated wall before being detached by buoyancy and driven into the liquid core, with weak tendency to flow with the liquid. The Wavy Vapor Layer Regime achieved at $\theta = 90°$ is the culmination of bubble coalescence into vapor patches that propagate along the heated wall mimicking a continuous wavy vapor layer. The Stratification Regime corresponding to $\theta = 180°$ is associated with stratification of vapor along the heated wall above the liquid. The Vapor Stagnation Regime captured at $\theta = 270°$ is the result of buoyancy force just balancing the drag force exerted by liquid on the vapor. Two additional low velocity CHF regimes not shown in Fig. 1(a) are Separated Concurrent Vapor Flow Regime that was encountered at velocities slightly greater than $U = 0.1$ m/s, where liquid drag begins to exceed buoyancy,

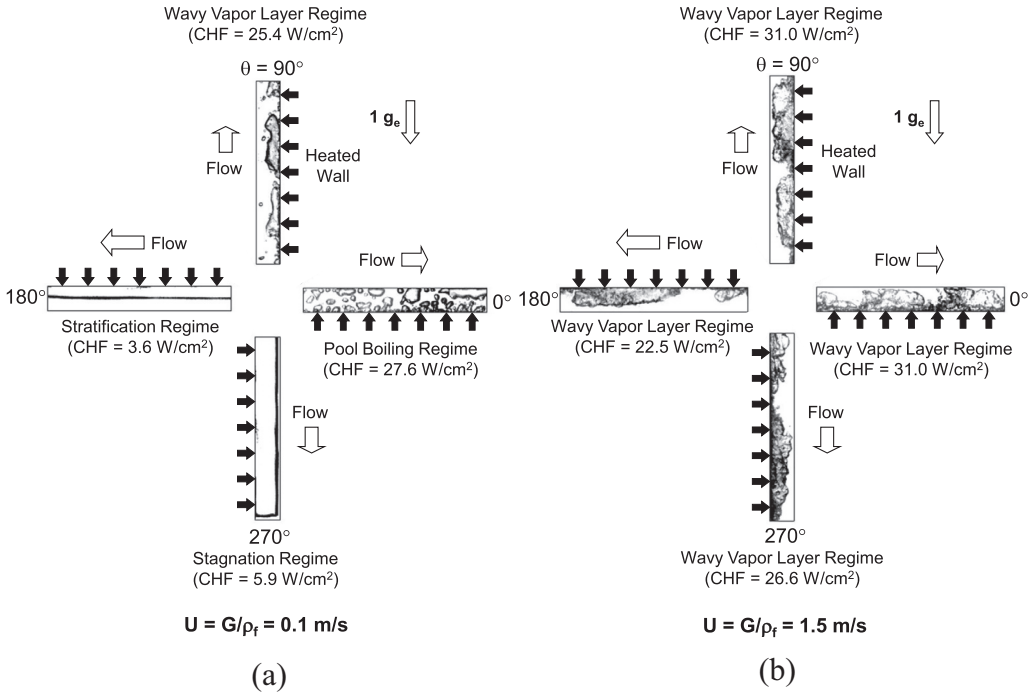

Fig. 1. Slightly subcooled ($\Delta T_{sub,o}$ = 3 °C) flow boiling CHF regimes at $1-g_e$ corresponding to different flow orientations for inlet liquid velocities (a) $U = G/\rho_f$ = 0.1 m/s and (b) $U = G/\rho_f$ = 1.5 m/s. CHF regime and magnitude are highly dependent on orientation for the lower velocity and independent of orientation for the higher velocity [37].

and Vapor Counter Flow Regime, captured at velocities below 0.1 m/s, where buoyancy exceeds liquid drag, pushing the vapor backwards towards the channel inlet. Fig. 1(b) depicts interfacial behavior at CHF− for slightly subcooled flow at U = 1.5 m/s. At this high velocity, CHF is dominated by inertia, which overcomes any buoyancy effects, resulting in all orientations yielding the same Wavy Vapor Layer Regime and fairly equal CHF values. Fig. 1(b) demonstrates the effectiveness of high velocity at overcoming body force effects.

Fig. 2(a) shows images of flow-boiling CHF obtained by Zhang et al. [42] in μg_e parabolic flight experiments. Unlike Fig. 1(a), which shows significant variations of CHF mechanism and magnitude at low velocity in $1-g_e$, the same Wavy Vapor Layer Regime is observed in μg_e regardless of flow velocity or subcooling. Fig. 2(b) shows interfacial behavior during the CHF transient in μg_e for slightly subcooled flow and U = 0.15 m/s. Just prior to CHF, vapor patches are shown propagating along the heated wall, taking the form of a wavy vapor layer. The heat is transferred from the wall to the bulk liquid in wetting fronts between the vapor patches. During the CHF transient, a wetting front is shown beginning to lift from the wall. At CHF+, all wettings fronts are detached from the wall, causing a continuous insulating wavy vapor layer to engulf the entire wall. This behavior is consistent with the Interfacial Lift-off CHF Model originally proposed by Galloway and Mudawar [23,24].

Fig. 2(c) depicts sequential images of flow boiling at low velocities and both low and high subcooling, which were obtained during hypergravity ($1.8-g_e$). The strong buoyancy force perpendicular to the heated wall is shown removing bubbles before they have the opportunity to coalesce with neighboring bubbles. Notice also that this boiling behavior mimics pool boiling at $1-g_e$. Strong condensation effects at high subcooling greatly reduce bubble size.

Fig. 2(d) shows the variations of CHF data by Zhang et al. [42] with velocity in μg_e and $1-g_e$ horizontal flow boiling. Notice how CHF in μg_e increases appreciably with increasing velocity, but the dependence is much weaker at $1-g_e$. At the lowest velocity, CHF in μg_e is only 50% of that at $1-g_e$. Increasing flow velocity is shown reducing differences between μg_e and $1-g_e$, with CHF values converging around 1.5 m/s. Fig. 2(d) also shows CHF predictions based on the Interfacial Lift-off Model. Since this model is intended specifically for flow boiling conditions fostering the Wavy Vapor Layer Regime, predictions are provided for the entire velocity range at μg_e, but only for high velocities at $1-g_e$, where the Wavy Vapor Layer Regime is observed.

1.5. Objectives of study

This study is the second part of a two-part study investigating flow boiling of FC-72 in μg_e, which is simulated in a series of parabolic flight maneuvers. The first part of this study [44] included findings from both high-speed video analysis of interfacial features and heat transfer measurements for different inlet velocities. This part of the study is focused on interfacial behavior associated specifically with flow boiling CHF, and development of a CHF model for a double-sided heated rectangular channel. This study is part of a NASA project with the goal of developing the Flow Boiling and Condensation Experiment (FBCE) for the International Space Station (ISS).

2. Experimental methods

Microgravity flow boiling experiments were performed onboard Zero-G Corporation's modified Boeing 727 parabolic flight aircraft. Details of the experimental methods used in this study are provided in the first part of this study, so only key aspects of these methods are highlighted. Shown in Fig. 3(a) is a schematic of the two-phase flow loop that is constructed to deliver FC-72 at the desired pressure, temperature and flow rate to the Flow Boiling Module (FBM). The FBM features transparent construction to facilitate high-speed video motion analysis of interfacial features. Fig. 3(b) shows key dimensions of the FBM: cross-sectional height of H = 5.0 mm and width of W = 2.5 mm, upstream development length of L_d = 327.9 mm, heated length of L_h = 114.6 mm, and exit

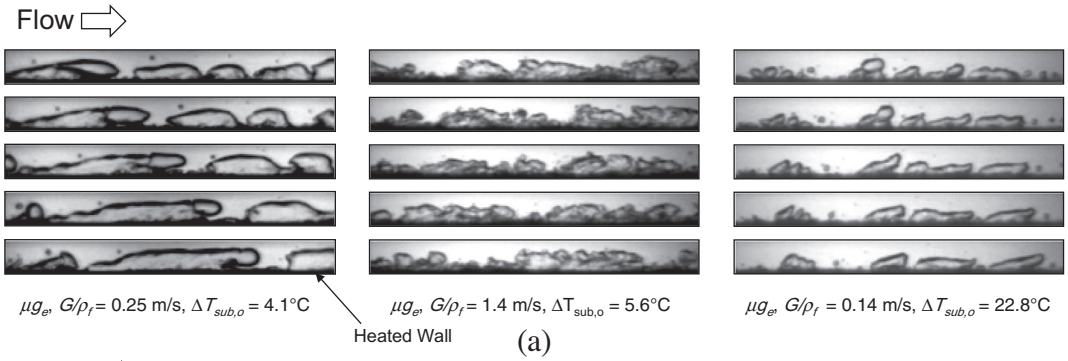

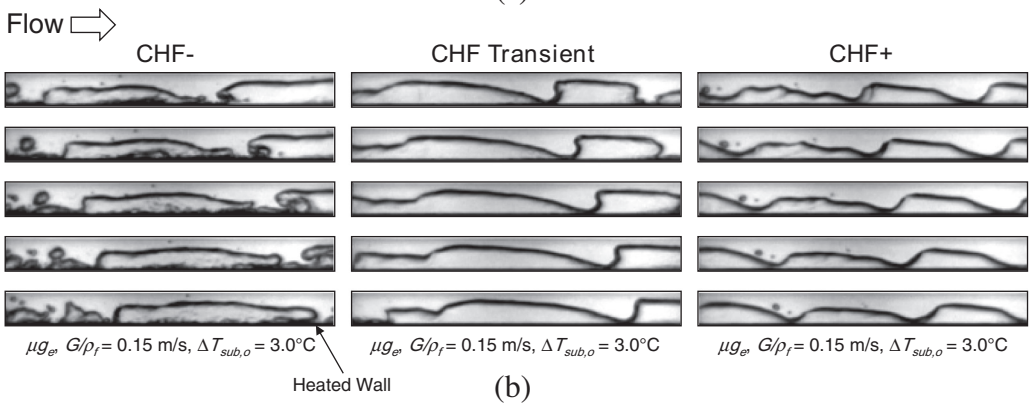

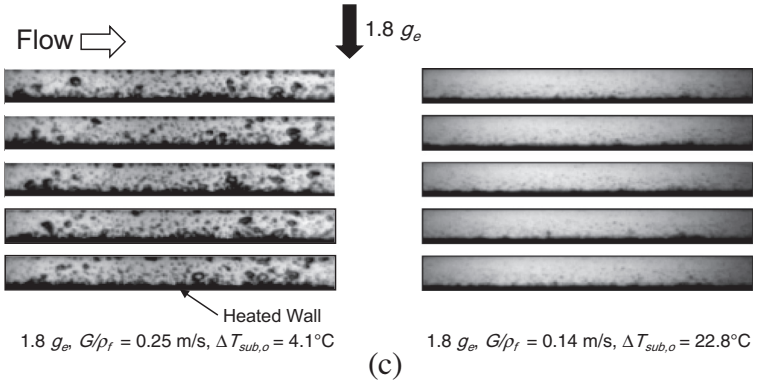

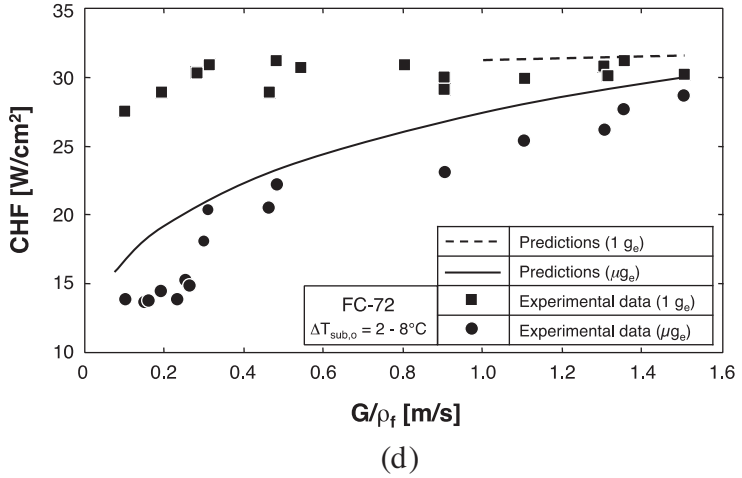

Fig. 2. Single-sided heating results [42]: (a) wavy vapor layer CHF regime prevalent in μg_e at both low and high velocities as well as slightly and highly subcooled conditions. (b) CHF transient in μg_e for G/ρ_f = 0.15 m/s and $\Delta T_{sub,o}$ = 3.0 °C. (c) Low velocity pool-boiling-like flow boiling at 1.8 – g_e. (d) Comparison of CHF data to predictions of Interfacial Lift-off Model.

length of L_e = 60.9 mm. The flow channel is fitted with two opposite copper heating walls along the smaller dimension (2.5 mm) of the cross-section. Heating is provided by a series of thick film resistors that are soldered to the backside of each copper wall. As

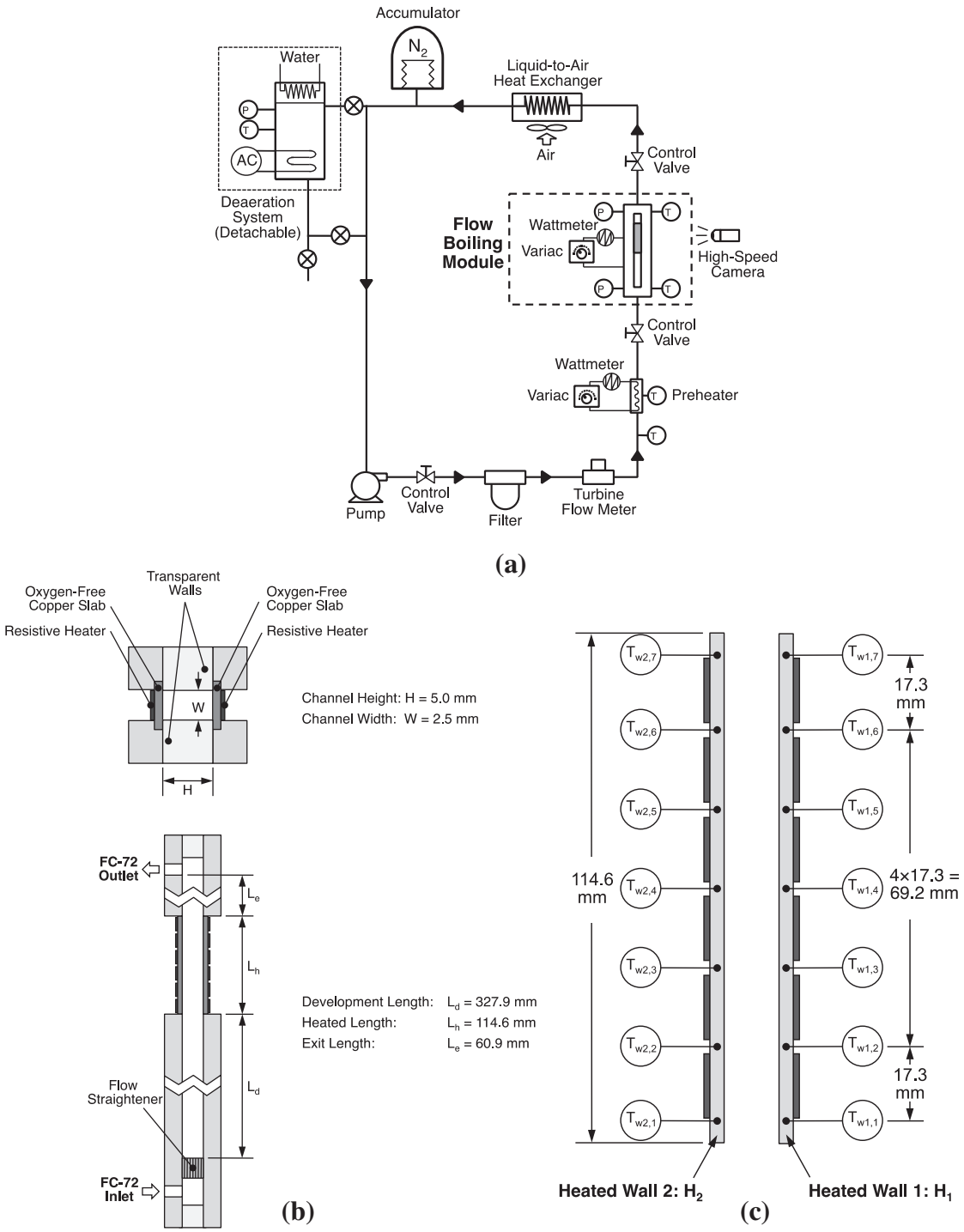

Fig. 3. (a) Schematic diagram of flow loop. (b) Key dimensions of flow channel. (c) Thermocouple layout in two heated walls.

shown in Fig. 3(c), Type-E thermocouples are inserted into shallow holes in each copper wall between the resistors. The thermocouples are designated by $T_{wm,n}$, where m represents the heated wall (H_1or H_2) and n the axial wall thermocouple location.

Four days of parabolic flight were dedicated to obtaining the data and video records presented in this study. The operating conditions are as follows: FC-72 inlet mean liquid velocity of U = 0.1–1.9 m/s, mass velocity of G = 224.2–3347.5 kg/m^2 s, inlet temperature of T_{in} = 56.5–64.7 °C, inlet subcooling of $\Delta T_{sub,in}$ = 2.8–8.1 °C, and outlet pressure of p_o = 118.2–148.3 kPa (17.1–21.5 psi).

3. Experimental results

3.1. Experimental pressure drop trends

Pressure drop is measured by STS absolute pressure transducers connected to taps in the channel immediately upstream and downstream of the copper heated walls. These pressures are measured continuously during every parabola with an accuracy of ±0.05%. The operator of the flow boiling facility can activate either one of the heated walls (H_1) or both walls (H_1 and H_2) simultaneously.

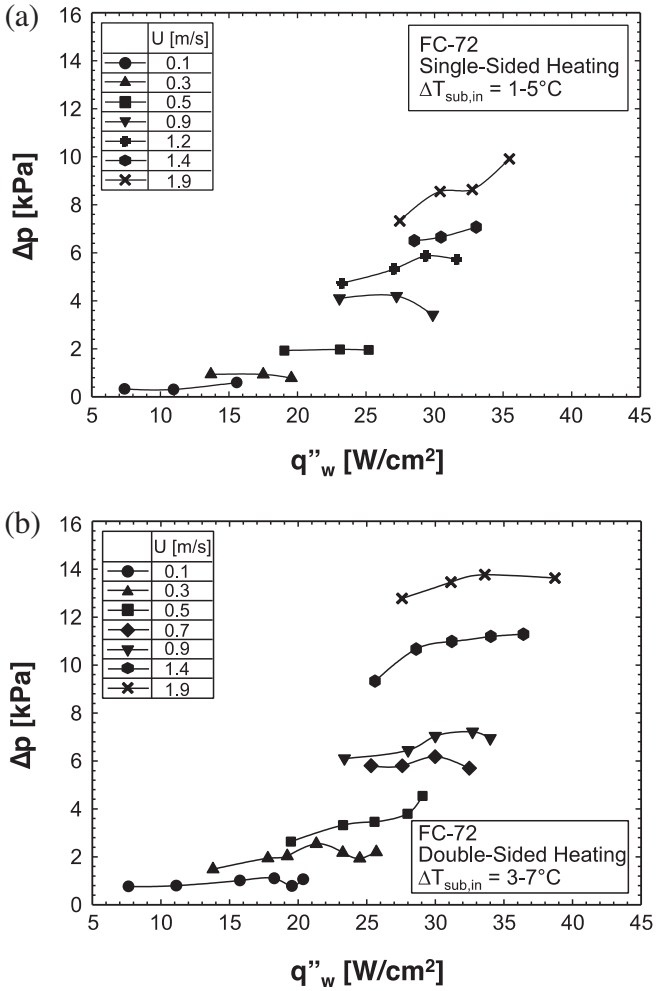

Fig. 4. Variation of pressure drop across the heated portion of the channel with wall heat flux for different inlet velocities for (a) single-sided heating and (b) double-sided heating.

Fig. 4(a) and (b) shows variations of the measured pressure drop, Δp, across the heated length, with wall heat flux for different inlet velocities for single-sided and double-sided heating, respectively. Table 1 shows values of measured pressure drop for both single-sided and double-sided heating at different operating conditions. Overall, Δp increases with increasing velocity for both heating configurations and, with less regularity, increases with increasing heat flux for a given velocity. However, double-sided heating produces greater pressure drop than single-sided heating for identical flow conditions. This is attributed to nearly twice the amount of vapor produced with double-sided heating greatly increasing the velocities of vapor and liquid.

Table 1
Measured pressure drop across heated channel for both single-sided and double-sided heating experiments.

U (m/s)	Δp (kPa) (Double-sided heating)	Δp (kPa) (Single-sided heating)
0.1	0.766–1.105	0.327–0.597
0.3	1.842–2.540	0.777–0.938
0.5	2.632–4.535	1.928–1.977
0.7	5.700–7.753	Not measured
0.9	6.104–7.219	3.423–4.200
1.2	Not measured	4.736–5.869
1.4	9.328–11.286	6.509–7.069
1.9	12.779–13.765	7.332–9.911

3.2. Video images of interfacial behavior at CHF

As discussed in the first part of the study [44], a high-speed camera is used to capture interfacial behavior along the entire heated portion of the channel. Also included in the first part is the detailed evolution of interfacial behavior preceding CHF for both single-sided and double-sided heating. Discussed below are interfacial features captured immediately preceding CHF commencement, during the CHF transient, and shortly after CHF. These results are used to lay the groundwork for formulation of a CHF model for flow boiling in μg_e.

Fig. 5 shows sequential images captured in μg_e during the CHF transient and immediately after CHF (CHF+) for single-sided heating at $U = 0.1$, 0.5, 0.9 and 1.9 m/s. The time elapsed between consecutive frames is 0.451 ms. This interfacial behavior agrees remarkably well with the μg_e flow boiling visualization results of Zhang et al. [42]. Fig. 5 shows the heated wall during the CHF transient at $U = 0.1$ m/s covered by broad vapor patches separated by short wetting fronts. As time elapses, the wetting fronts sustaining heat transfer from the wall to the bulk liquid as well as liquid replenishment of the wall are gradually lifted from the wall. At CHF+, boiling activity in the wetting fronts appears to be fully extinguished, causing the heated wall to be completely encased by a continuous wavy vapor layer. Increasing the flow velocity to $U = 0.5$ m/s is shown decreasing the wavy vapor layer's mean thickness and wavelength while increasing the number of wetting fronts along the heated wall. The trends of decreasing mean thickness and wavelength, and increasing number of wetting fronts is evident at the two highest flow velocities of $U = 0.9$ and 1.9 m/s. The most noticeable change in interfacial behavior between the CHF transient and CHF+ is the gradual extinguishing of boiling activity in the wetting fronts. It appears that an initial wetting front is extinguished first, causing the same total amount of heat to be dissipated through a smaller number of wetting fronts. This causes the remaining wetting fronts to be extinguished even more rapidly. This chain reaction eventually culminates in the loss of cooling in all wetting fronts.

Fig. 6 depicts sequential images captured in μg_e just before CHF(CHF−), during the CHF transient, and just after CHF (CHF+) for double-sided heating at $U = 0.1$, 0.5, 0.9 and 1.9 m/s, where CHF− corresponds to heat fluxes equal to 95 ± 1% of CHF value. Notice that the image sequences for the single-sided heating do not include CHF- because coarse heat flux increments during these tests caused the last pre-CHF value to fall below the 95 ± 1% range. The double-sided tests involved far smaller heat flux increments prior to CHF, allowing precise determination of CHF− conditions, as well as measurement of CHF values for both heated walls. For double-sided heating, Fig. 6 shows CHF− for $U = 0.1$ m/s is associated with the development of wavy vapor layers starting immediately at the leading edge of the heated region. There is also appreciable meshing between wavy vapor layers from the opposite walls beginning near the leading edge, whereas the downstream region incurs merging of the wavy vapor layers, with both walls being replenished by liquid ligaments that are entrained in the coalescent vapor flow. During the CHF transient, majority of the downstream region is covered with vapor, and cooling is concentrated in a few wetting fronts farther upstream. At CHF+, these upstream wetting fronts are extinguished, meaning no further regions are available for core liquid to cool or replenish the heated walls. As the inlet velocity is increased to 0.5 and 0.9 m/s, the mean thickness of the opposite wavy vapor layers decreases at CHF−, shifting both the meshing and merging of the two layers farther downstream; there is also a substantial increase in the number of wetting fronts. During the CHF transient, downstream regions begin to dry out, and, at CHF+, wetting fronts both upstream and in the middle of the heated region begin to be extinguished. At

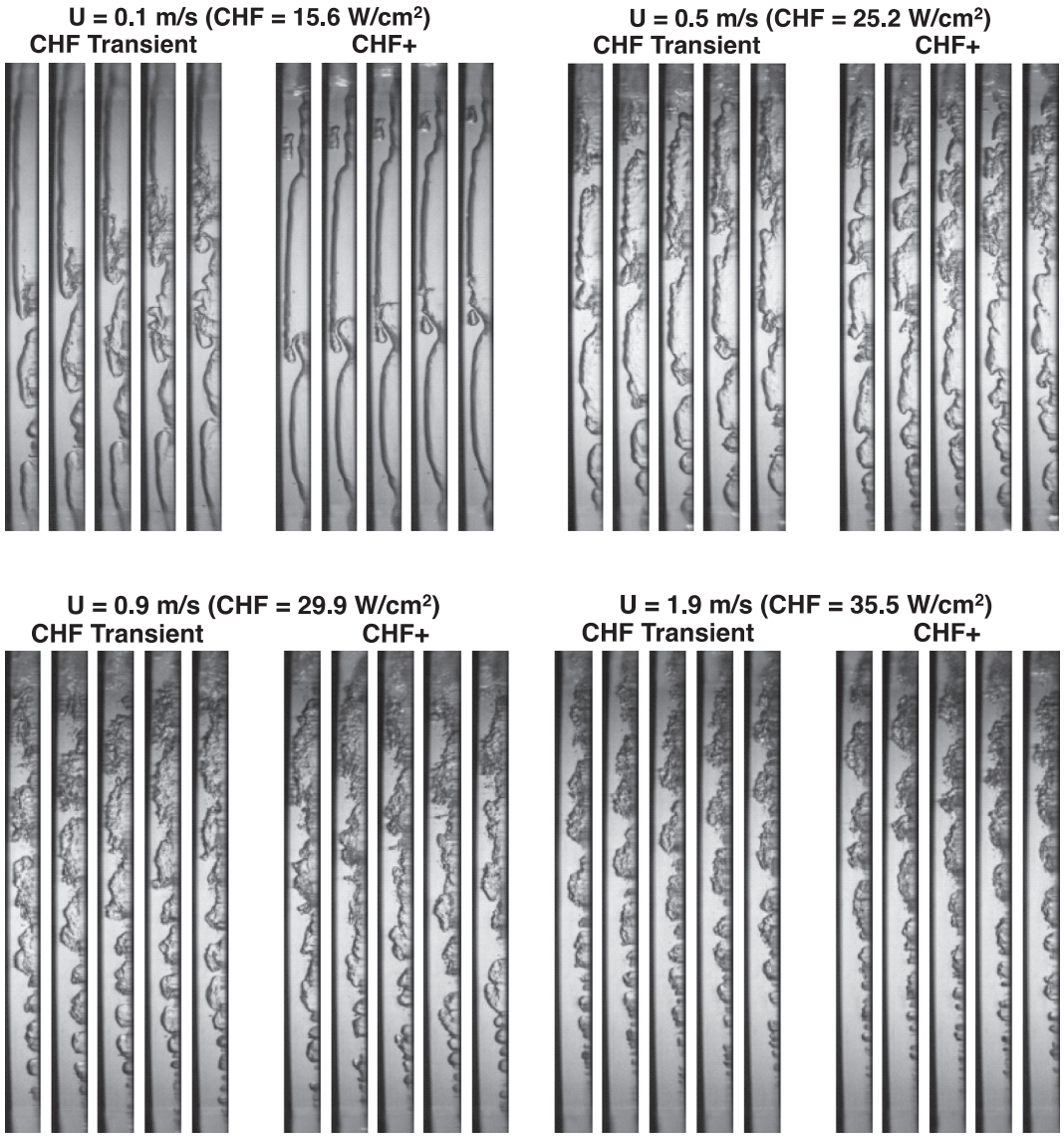

Fig. 5. Sequential high-speed video images from single-sided heating experiments for different inlet velocities obtained during CHF transient and at CHF+.

the highest inlet velocity of U = 1.9 m/s, CHF− conditions could not be captured by video within the 95 ± 1% range, but images during the CHF transient depict a substantial decrease in mean thickness of the opposite vapor layers and increase in the number of wetting fronts; the meshing between the two layers is also shifted farther downstream compared to lower velocities. At CHF+, there is downstream merging between the two layers and difficulty maintaining wetting fronts; both appear to contribute to wall dryout.

3.3. Idealized representation of interfacial behavior at CHF−

Fig. 7(a) and (b) shows idealized schematics of interfacial behavior observed at CHF− in the upstream region for single-sided and double-sided heating, respectively. A key feature of the interfacial behavior for both configurations is wavy vapor layer formation. This vapor layer is the result of both evaporation and bubble coalescence. Localized dryout occurs beneath the wave peaks as the wavy vapor layer propagates along the heated wall, while vigorous boiling is sustained in wetting fronts corresponding to the wave troughs. There is also a continuous wetting front upstream. The mean thickness of the wavy vapor layer increases along the flow direction due to evaporation. Notice that the meshing and merging of vapor layers from opposite walls for double-sided heating are purposely eliminated from Fig. 7(b) to better represent the upstream evolution of the wavy vapor layer and wetting fronts as a prelude to development of the CHF model in the next section. The meshing and merging phenomena are depicted in Fig. 9(b) of the first part of this study [44].

4. CHF model

4.1. Model rationale

Aside from the present findings, the CHF model presented in this section is also based on extensive photographic evidence from past $1-g_e$ [23,24,37–39,45–53] and μg_e flow boiling studies [42,43]. In all these studies, flow boiling was investigated along rectangular channels that were heated along a single wall. The most dominant interfacial feature observed in all these studies is a periodic wavy vapor layer that develops along the heated wall prior to CHF. The interfacial waviness is clearly a manifestation of hydrodynamic instability between liquid and vapor layers

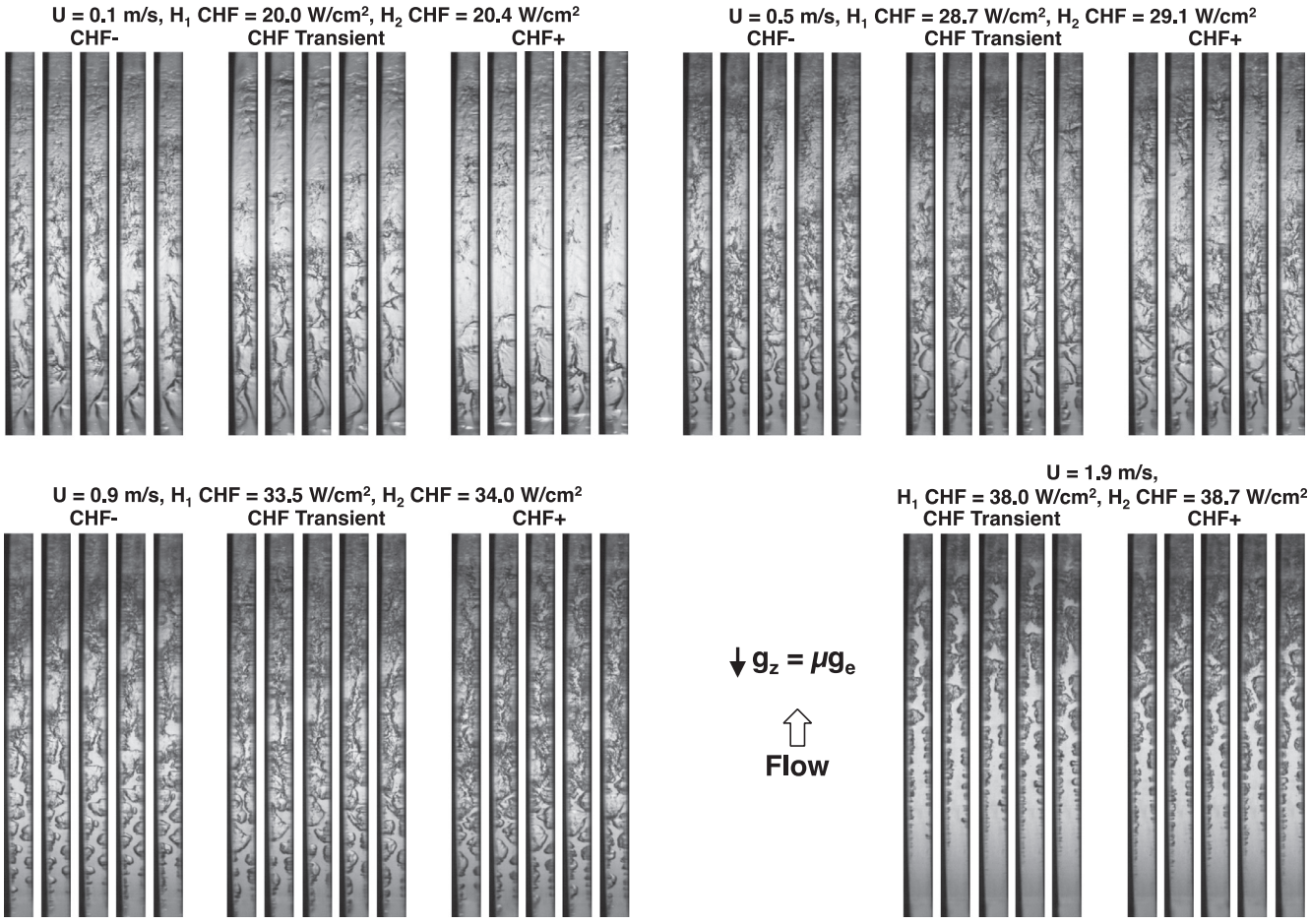

Fig. 6. Sequential high-speed video images from double-sided heating experiments for different inlet velocities obtained at CHF−, during CHF transient and at CHF+.

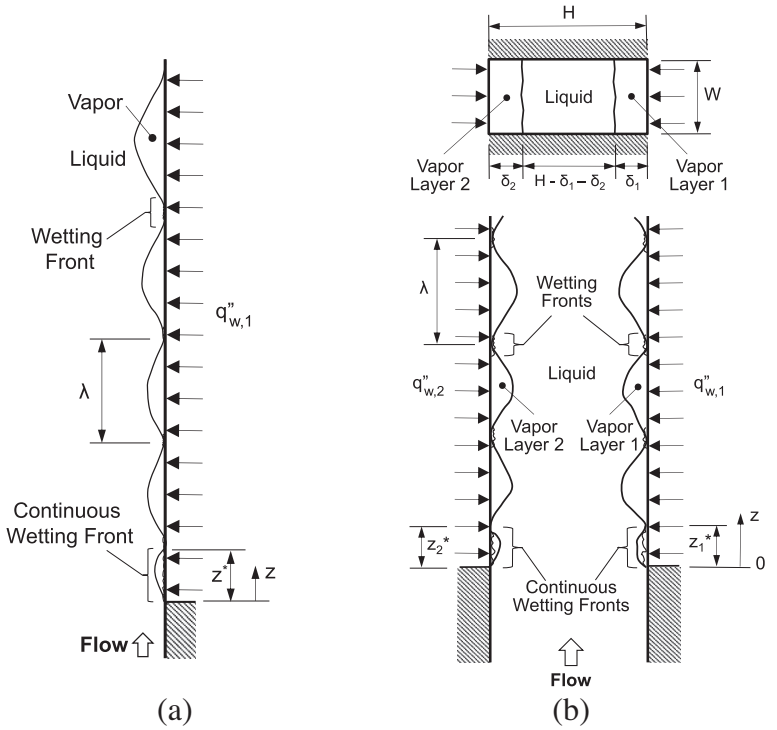

Fig. 7. Schematics of upstream wavy vapor layer and wetting front development at CHF- for (a) single-sided heating and (b) double-sided heating. Downstream meshing and merging of vapor layers from the opposite walls for double-sided heating are purposely eliminated to better represent the upstream development of the vapor layers.

moving at different velocities. The second dominant feature is contact of the wavy interface with the wall in discrete "wetting fronts" corresponding to the wave troughs. At CHF−, vigorous boiling is observed in the wetting front, while portions of the vapor layer around the wave peaks appear dry. This feature points to the wetting fronts as the last source for cooling and liquid replenishment for the heated wall. Two forces control the formation of a wetting front. A pressure force associated with interfacial curvature around the wave troughs pushes the interface towards the heated wall. The pressure force is opposed by momentum generated by intense vapor effusion in the wetting front normal to, and away from the wall. Interfacial contact with the wall is ensured and wetting fronts are maintained at CHF− because the pressure force exceeds the vapor momentum. CHF is postulated to commence when the vapor momentum increases to just overcome the pressure force. This event causes lifting of the interface from the wall, which extinguishes the wetting front. Heat that was dissipated at the just extinguished wetting front must now be conducted axially through the wall and dissipated to neighboring wetting fronts. This increases the momentum of vapor effusion in the neighboring wetting fronts, fostering rapid extinguishing of these wetting fronts as well. This process can best be described as a chain reaction, where wetting fronts are extinguished in succession and at an increasing rate. Loss of wetting fronts leaves the wall essentially dry, an event that is captured by the wall thermocouples in the form of a sharp and unsteady rise in the wall temperature. These interfacial events at CHF− are key components of the Interfacial Lift-off Model first proposed by Galloway and Mudawar [23,24] for single-sided heating.

However, the model sought here must tackle double-sided heating and accurately predict data for both $1-g_e$ and μg_e. Like the original Galloway and Mudawar model, the present model incorporates four major components: (1) a separated flow model to determine axial variations of mean liquid and vapor velocities, and mean thickness of the wavy vapor layers, (2) an instability model of the wavy vapor layer to determine the wavelength, wetting front axial span, and pressure force created by interfacial curvature, (3) an Interfacial Lift-off Criterion – CHF trigger mechanism – to determine the heat flux in wetting fronts required to produce sufficient vapor momentum to exceed the curvature pressure force, and (4) a surface energy balance to relate the average wall heat flux for the entire heated wall to the heat flux concentrated in the wetting fronts propagating along the wall.

4.2. Separated flow model

A separated flow model is constructed to determine axial variations of mean liquid and vapor velocities, and mean thickness of the wavy vapor layers. Illustrated in Fig. 8(a) is an idealized representation of vapor layers growing along both heated walls with the liquid flowing in between. The flow, therefore, consists of three clearly identifiable layers. The control volume method is used to apply mass, momentum and energy conservation to the individual phases and/or the entire flow. In Fig. 8(a), $\Gamma_{fg,1}$ and u_{i1} represent the rate of evaporation per unit distance between the liquid layer and vapor layer 1, and streamwise velocity of the liquid–vapor interface in between. Similarly, $\Gamma_{fg,2}$ and u_{i2} represent the rate of evaporation per unit distance between the liquid layer and vapor layer 2 and the streamwise velocity of the liquid–vapor interface in between. The assumptions employed in the separated flow model are: (1) the heated walls provide equal heat fluxes, (2) the vapor layers are initiated at the leading edge ($z = 0$) for each heated wall (this assumption is justified by the slightly subcooled inlet liquid conditions), (3) velocities are uniform across the individual layers (*i.e.*, the two-phase flow is one-dimensional), (4) pressure is uniform across the channel's cross-section, (5) the middle liquid layer preserves its subcooling in the axial direction, and (6) the vapor maintains saturation temperature corresponding to local pressure at every z location.

Applying mass conservation to a control volume of length Δz encompassing the entire cross-section yields $d\dot{m}/dz = 0$, which implies $\dot{m}$ is constant, also G is constant since $G = \dot{m}/A$ and A is constant. Applying energy conservation to the vapor layers yields the following relations for mean velocities, U_{g1} and U_{g2}, of the vapor layers along heated walls H_1 and H_2, respectively, in terms of the mean thicknesses of the respective layers,

$$U_{g1} = \frac{q''_w z}{\rho_g \delta_1 \left(c_{p,f}\Delta T_{sub,in} + h_{fg}\right)} \tag{1a}$$

$$\text{and} \quad U_{g2} = \frac{q''_w z}{\rho_g \delta_2 \left(c_{p,f}\Delta T_{sub,in} + h_{fg}\right)} \tag{1b}$$

Continuity is used to derive an expression for the mean velocity of the liquid layer. For equal heat flux, q''_w, applied along both heated walls,

$$U_f = \frac{UH}{H-\delta_1-\delta_2} - \frac{2q''_w z}{\rho_f (H-\delta_1-\delta_2)\left(c_{p,f}\Delta T_{sub,in} + h_{fg}\right)}. \tag{2}$$

Fig. 8(b) shows momentum conservation for control volumes of length Δz encompassing the three individual layers of the flow. For now, an arbitrary gravitational acceleration, g, is assumed with the channel oriented at angle θ relative to the horizontal plane, and $g \approx 0$ in microgravity. Summing momentum and force terms yields the following relations for heated wall vapor layer 1, liquid layer and heated wall vapor layer 2, respectively,

$$\frac{d}{dz}\left(\rho_g U_{g1}^2 A_{g1}\right) - \Gamma_{fg1} u_{i1} = -A_{g1}\frac{dp}{dz} - \tau_{w,g1}P_{w,g1} \mp \tau_{i1}P_{i1} - \rho_g A_{g1} g \sin\theta, \tag{3a}$$

$$\frac{d}{dz}\left(\rho_f U_f^2 A_f\right) + \Gamma_{fg1} u_{i1} + \Gamma_{fg2} u_{i2} = -A_f\frac{dp}{dz} - \tau_{w,f}P_{w,f} \pm \tau_{i1}P_{i1} \pm \tau_{i2}P_{i2} - \rho_f A_f g \sin\theta, \tag{3b}$$

$$\text{and} \quad \frac{d}{dz}\left(\rho_g U_{g2}^2 A_{g2}\right) - \Gamma_{fg2} u_{i2} = -A_{g2}\frac{dp}{dz} - \tau_{w,g2}P_{w,g2} \mp \tau_{i2}P_{i2} - \rho_g A_{g2} g \sin\theta \tag{3c}$$

where A_{g1}, A_f, A_{g2}, u_{i1}, u_{i2}, $\tau_{w,g1}$, $\tau_{w,f}$, $\tau_{w,g2}$, $P_{w,g1}$, $P_{w,f}$, $P_{w,g2}$, τ_{i1}, τ_{i2}, P_{i1}, and P_{i2} are the flow area for vapor layer 1, flow area for the liquid layer, flow area for vapor layer 2, interfacial velocity between vapor layer 1 and the liquid layer, interfacial velocity between vapor layer 2 and the liquid layer, wall shear stress for vapor layer 1, wall shear stress for the liquid layer, wall shear stress for vapor layer 2, wall friction perimeter for vapor layer 1, wall friction perimeter for the liquid layer, wall friction perimeter for vapor layer 2, interfacial shear stress between vapor layer 1 and the liquid layer, interfacial shear stress between vapor layer 2 and the liquid layer, interfacial perimeter between vapor layer 1 and the liquid layer, and interfacial perimeter between vapor layer 2 and the liquid layer. The flow areas are defined in Fig. 8(a) in terms of the channel dimensions (W and H) and thicknesses of vapor layer 1, δ_1, and vapor layer 2, δ_2. Fig. 8(b) provides definitions for all wall friction and interfacial perimeters.

Visual observations from prior flow boiling studies [42,43] revealed the vapor generated at the leading edge of the heated wall has no initial streamwise velocity. Therefore, it is assumed the liquid–vapor interface does not contribute streamwise momentum to the control volumes ($u_{i1} = u_{i2} = 0$). Eqs. (3a)–(3c) can be presented in terms of flow quality of vapor layer 1, x_1, void fraction

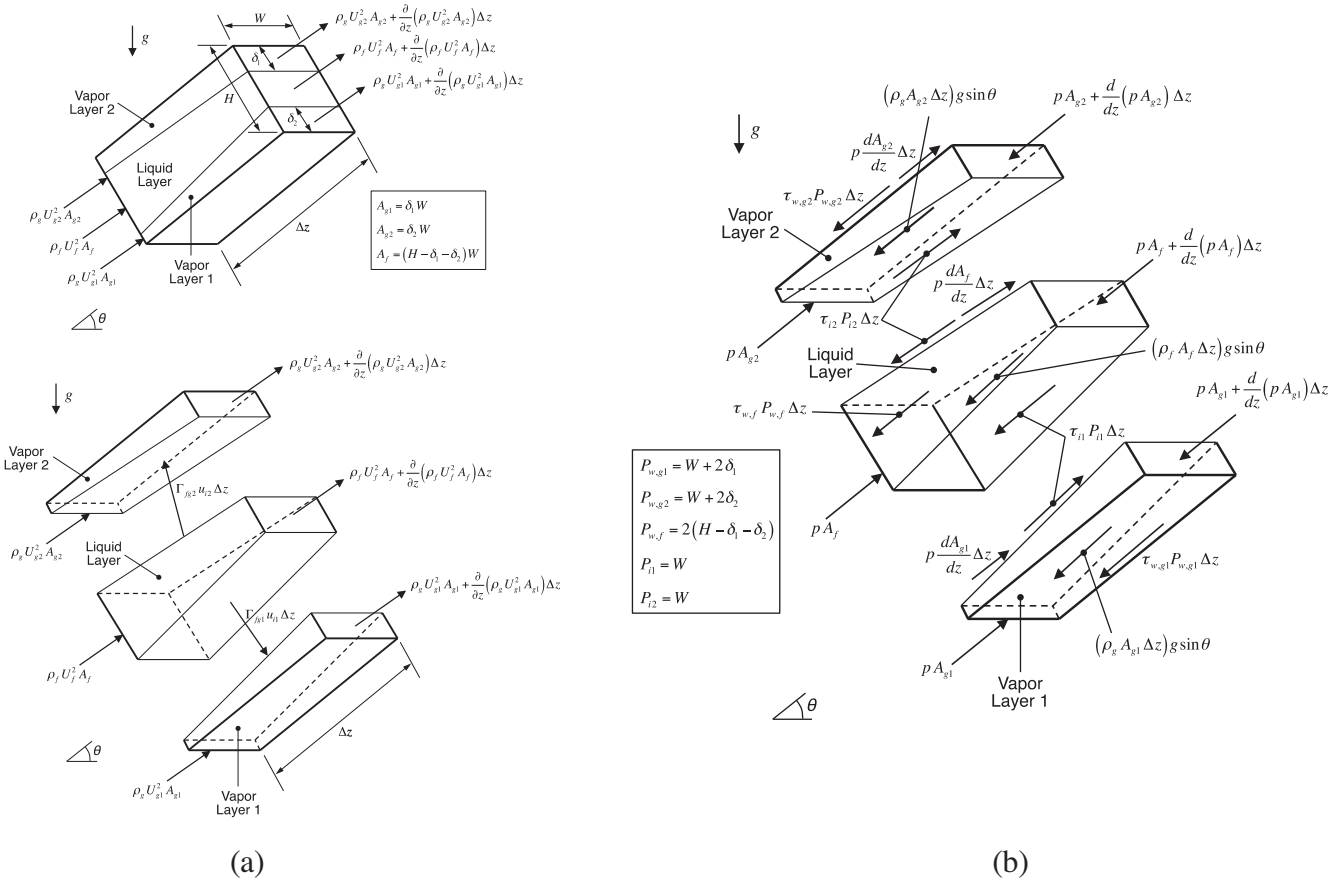

Fig. 8. (a) Momentum conservation applied to control volumes of length Δz for combined two-phase flow and for individual layers. (b) Force terms pertaining to control volumes of individual layers.

of vapor layer 1, α_1, flow quality of vapor layer 2, x_2, and void fraction of vapor layer 2, α_2:

$$G^2\frac{d}{dz}\left[\frac{x_1^2}{\rho_g\alpha_1}\right] = -\alpha_1\frac{dp}{dz} - \frac{\tau_{w,g1}P_{w,g1}}{A} \mp \frac{\tau_{i1}P_{i1}}{A} - \rho_g\alpha_1 g\sin\theta, \tag{4a}$$

$$G^2\frac{d}{dz}\left[\frac{(1-x_1-x_2)^2}{\rho_f(1-\alpha_1-\alpha_2)}\right] = -(1-\alpha_1-\alpha_2)\frac{dp}{dz} - \frac{\tau_{wf}P_{wf}}{A} \pm \frac{\tau_{i1}P_{i1}}{A} \pm \frac{\tau_{i2}P_{i2}}{A} - \rho_f(1-\alpha_1-\alpha_2)g\sin\theta,$$

$$\text{and}\quad G^2\frac{d}{dz}\left[\frac{x_2^2}{\rho_g\alpha_2}\right] = -\alpha_2\frac{dp}{dz} - \frac{\tau_{w,g2}P_{w,g2}}{A} \mp \frac{\tau_{i2}P_{i2}}{A} - \rho_g\alpha_2 g\sin\theta, \tag{4c}$$

where $A = WH$ and the definitions for x_1, α_1, x_2, α_2, $\tau_{w,g1}$, $\tau_{w,f}$, $\tau_{w,g2}$, τ_{i1} and τ_{i2} are provided in Table 2.

Notice that, for equal heat flux, q''_w, along both heated walls, Eqs. 1(a) and 1(b) yield the following differential relations for flow qualities of the vapor layers:

$$\frac{dx_1}{dz} = \frac{dx_2}{dz} = \frac{q''_w W}{\dot{m}\left(c_{p,f}\Delta T_{sub,in} + h_{fg}\right)}. \tag{5}$$

Using a fourth-order Runge–Kutta numerical scheme, the separated flow model relations are solved simultaneously to determine axial variations of pressure, p, qualities, x_1 and x_2, mean velocity of vapor layer 1, U_{g1}, mean velocity of liquid velocity, U_f, mean velocity of vapor layer 2, U_{g2}, mean thickness of vapor layer 1, δ_1, and mean thickness of vapor layer 2, δ_2. The main input parameters of the model equations, which are defined at the inlet to the channel's heated length ($z = 0$) are inlet pressure, p_{in}, inlet temperature, T_{in}, mass velocity, G, and wall heat flux, q''_w.

4.3. Interfacial instability analysis

Visual observations from prior flow boiling studies corresponding to subcooled [23,24,37–43,45–48] and saturated [49–52] inlet conditions, showed the vapor at CHF– forms a wavy layer along the heated wall. Classical instability theory [24,55,56] is utilized to describe a sinusoidal liquid–vapor interface between two fluid layers moving at different velocities. The instability is governed by the relative influences of the inertia, surface tension and body force. Instability is postulated to be a necessary condition for the interface to contact the heated wall in order to establish wetting fronts. In the analysis presented below, hydrodynamic instability analysis is used to determine (1) the wavelength of the vapor–liquid interface, which also dictates the length of the wetting fronts, and (2) the interfacial curvature above the wetting front, which dictates the magnitude of pressure force tending to secure attachment of the interface with the heated wall. Similar instability analysis has yielded remarkable success in predicting flow boiling CHF for single-sided heating [24,37–39,42,43,46,48–52].

Fig. 9(a) and (b) shows idealized instability representations of flow boiling at CHF- in Earth's gravity and microgravity, respectively. The vapor–liquid interfaces between vapor layer 1 and the liquid layer, and between vapor layer 2 and the liquid layer, are assumed to acquire the simple waveform $\eta(z,t) = \eta_0 e^{ik(z-ct)}$, where η_0 is the wave amplitude, k the wave number ($k = 2\pi/\lambda$), and c the

Table 2
Summary of relations used in conjunction with the separated flow model.

Quality relations for individual vapor layers

$x_1 = \frac{\rho_g U_{g1} \alpha_1}{G}$ and $x_2 = \frac{\rho_g U_{g2} \alpha_2}{G}$

Wall shear stress relations

$$\tau_{w,k,m} = \frac{1}{2}\rho_k U_{k,m}^2 f_{k,m}$$

$$f_{k,m} = C_1 + \frac{C_2}{Re_{D,k,m}^{1/C_3}} = C_1 + \frac{C_2}{\left(\frac{\rho_k U_{k,m} D_{k,m}}{\mu_k}\right)^{1/C_3}}$$

where $k = f$ or g, and $m = 1$–2. $C_1 = 0$, $C_2 = 16$ and $C_3 = 1$ for laminar flow ($Re_{D,k,m} \leqslant 2100$), $C_1 = 0.0054$, $C_2 = 2.3 \times 10^{-8}$ and $C_3 = -2/3$ for transitional flow ($2100 < Re_{D,k,m} \leqslant 4000$), and $C_1 = 0.00128$, $C_2 = 0.1143$ and $C_3 = 3.2154$ for turbulent flow ($Re_{D,k,m} > 4000$) [54], where $D_{k,m} = 4A_{k,m}/P_{k,m}$

Interfacial shear stress relations

$\tau_{i1} = \frac{C_{f,i}}{2}\rho_g (U_{g1} - U_f)^2$ and $\tau_{i2} = \frac{C_{f,i}}{2}\rho_g (U_{g2} - U_f)^2$,
where $C_{f,i} = 0.5$ [24]

wave speed. The wave speed is comprised of a real part, representing actual speed of the interface, and an imaginary part that characterizes interfacial stability, $c = c_r + ic_i$. A disturbance normal to the interface associated with this waveform produces a pressure difference across the interface that can be expressed as

$$p_f - p_g = -\left[\rho_f''(c - U_f)^2 + \rho_g''(c - U_g)^2 + \left(\rho_f - \rho_g\right)\frac{g_n}{k}\right] k\eta_o e^{ik(z-ct)}, \tag{6}$$

where $\rho_f'' = \rho_f \coth(kH_f)$ and $\rho_g'' = \rho_g \coth(kH_g)$ are "modified density" terms, and g_n is the component of gravity normal to the heated wall. Eq. (6) represents instability between a single liquid layer and single vapor layer, which is why the subscripts for heated walls H_1 and H_2 in mean vapor velocity are dropped for now. The mean liquid and vapor thicknesses, H_f and H_g, respectively, found in the modified density terms are obtained from the simple relations

$$H_g = \delta_1 = \delta_2 = \delta, \tag{7a}$$

and $$H_f = H - \delta_1 - \delta_2 = H - 2\delta, \tag{7b}$$

which assume identical vapor behavior on both heated walls. Pressure difference across the vapor–liquid interface can also be approximated as the product of surface tension and curvature,

$$p_f - p_g \approx \sigma\frac{\partial^2 \eta}{\partial z^2} = -\sigma\eta_o k^2 e^{ik(z-ct)}. \tag{8}$$

Equating Eqs. (6) and (8) for pressure difference yields the following quadratic equation for wave speed,

$$\rho_f''(c - U_f)^2 + \rho_g''(c - U_g)^2 + \left(\rho_f - \rho_g\right)\frac{g_n}{k} - \sigma k = 0, \tag{9}$$

whose solution is

$$c = \frac{\rho_f'' U_f + \rho_g'' U_g}{\rho_f'' + \rho_g''} \pm \sqrt{\frac{\sigma k}{\rho_f'' + \rho_g''} - \frac{\rho_f''\rho_g''(U_g - U_f)^2}{\left(\rho_f'' + \rho_g''\right)^2} - \frac{\left(\rho_f - \rho_g\right)}{\left(\rho_f'' + \rho_g''\right)}\frac{g_n}{k}}. \tag{10}$$

The terms under the radical in Eq. (10) represent different momentum and force components. The wave speed will acquire both real and imaginary components when the sum of terms under the radical is negative. The real and imaginary components can be expressed, respectively, as

$$c_r = \frac{\rho_f'' U_f + \rho_g'' U_g}{\rho_f'' + \rho_g''} \tag{11a}$$

and $$c_i = \sqrt{\frac{\rho_f''\rho_g''(U_g - U_f)^2}{\left(\rho_f'' + \rho_g''\right)^2} + \frac{\left(\rho_f - \rho_g\right)}{\left(\rho_f'' + \rho_g''\right)}\frac{g_n}{k} - \frac{\sigma k}{\rho_f'' + \rho_g''}}. \tag{11b}$$

In Eq. (11b), the first term under the radical accounts for inertial, which is always destabilizing to the interface. The second term is associated with the gravitational body force, which in Earth's gravity may be stabilizing or destabilizing depending on orientation of the heated wall relative to gravity, while $g_n \approx 0$ in microgravity. The third term accounts for surface tension force, which tends to stabilize the interface.

The interface is stable when $c_i < 0$, which causes the amplitude of interfacial perturbation to decrease with time, preventing any contact of the interface with the heated surface. The interfacial contact essential to producing the wetting fronts requires that $c_i > 0$. Neutral stability, or the condition that initiates the contact is achieved when $c_i = 0$. The neutral stability condition is used to determine the value of critical wave number, k_c, associated with the critical wavelength, λ_c. This is achieved by setting Eq. (11b) equal to zero,

$$k_c = \frac{2\pi}{\lambda_c} = \frac{\rho_f''\rho_g''(U_g - U_f)^2}{2\sigma\left(\rho_f'' + \rho_g''\right)} + \sqrt{\left[\frac{\rho_f''\rho_g''(U_g - U_f)^2}{2\sigma\left(\rho_f'' + \rho_g''\right)}\right]^2 + \frac{\left(\rho_f - \rho_g\right)g_n}{\sigma}}. \tag{12}$$

Aside from the magnitude of body force, there are fundamental differences between double-sided heating in microgravity and at different orientations in Earth gravity. In the latter, the components of gravity perpendicular to the heated walls yield different instability behavior for the two vapor layers. As shown in Fig. 9(a), the gravitational components normal to the upward-facing heater (1) and the downward-facing heater (2) are expressed, respectively, as

$$g_{n,1} = g_e \cos\theta, \tag{13a}$$

and $$g_{n,2} = g_e cos(\theta + \pi) = -g_e \cos\theta. \tag{13b}$$

For a particular flow orientation θ, the gravitational body force tends to destabilize the liquid–vapor interface adjacent to the upward-facing heated wall, and stabilize the interface on the downward-facing heated wall. Therefore, the interface along the downward-facing wall will be either stable or unstable, but with a critical wavelength larger than that of the upward-facing wall. For an unstable interface along the downward-facing wall, curvature near the wetting fronts is also weaker, causing CHF to be lower

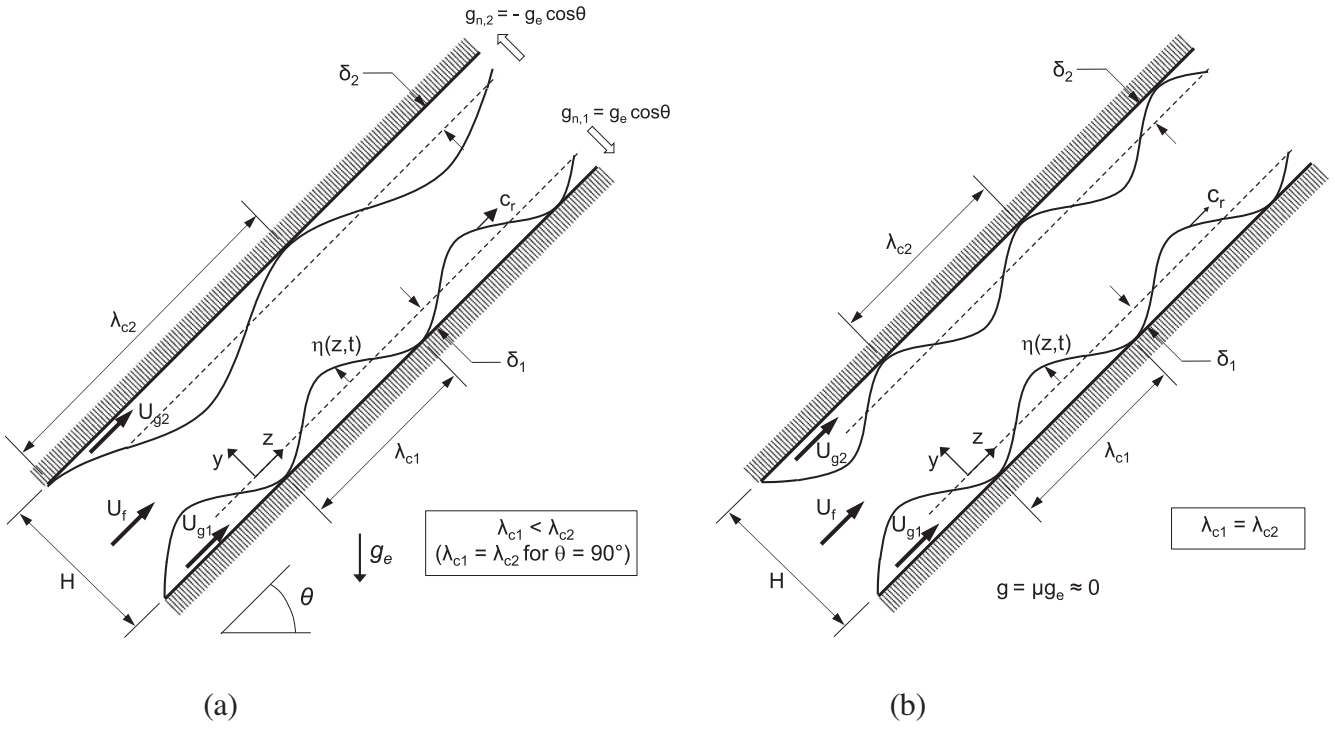

Fig. 9. Hydrodynamic instability of wavy vapor layers along heated walls of double-sided heated channel at CHF– (a) for inclined channel at $1 - g_e$ and (b) for microgravity.

for the downward-facing wall compared to the upward-facing. It is important to note that these effects are more pronounced for low inlet velocities, where the influence of body force is most significant. However, by greatly increasing the inlet velocity, body force effects become comparatively insignificant, and CHF differences between the two walls less discernible. Notice that in Earth's gravity, vertical upflow produces zero gravitational body forces normal to the opposite heated walls and equal CHF values for both walls.

In microgravity, the body force component is negligible, which reduces Eq. (12) to

$$\lambda_c = \frac{2\pi\sigma\left(\rho_f'' + \rho_g''\right)}{\rho_f''\rho_g''\left(U_g - U_f\right)^2}. \tag{14}$$

Also, in the absence of gravity, CHF is the same for the two opposite heated walls. Flow visualization results from [37–43] have demonstrated the existence of a continuous upstream liquid wetting region, z^*, defined as

$$z^* = z_0 + \lambda_c(z^*), \tag{15}$$

where z_0 is the distance from the leading edge of the heated wall to the location where the vapor velocity just exceeds the liquid velocity. Beyond z^*, the vapor velocity continues to increase faster than the liquid velocity, resulting in hydrodynamic instability of the wavy vapor–liquid interface. Determination of λ_c using Eq. (14) and z^* using Eq. (15) requires iteration. The separated flow model provides the flow parameters required to calculate critical wavelength.

4.4. Interfacial Lift-off Criterion

As discussed earlier, CHF is postulated to occur when the momentum of vapor emanating in the wetting fronts normal to the heated wall overcomes the pressure force associated with interfacial curvature. Illustrated in Fig. 10(a), the average pressure force over the wetting front is equated to the vapor momentum. Integrating the expression for pressure difference, Eq. (8), over the width of the wetting front, $b\lambda$,

$$\overline{p_f - p_g} = \frac{4\pi\sigma\delta}{b\lambda_c^2}\sin(b\pi), \tag{16}$$

where b is the ratio of wetting front length to the wavelength. Extensive video analysis of the wavy vapor layer at CHF– by Sturgis and Mudawar [47,48] revealed a consistent value of $b = 0.2$, which also used in the present study. The mean velocity of vapor produced in the wetting front normal to the heated wall is obtained by equating the heat concentrated in the wetting front to the energy of the generated vapor:

$$q_{w,w}'' A_{w,w} = \left(c_{p,f}\Delta T_{sub,in} + h_{fg}\right)\rho_g U_{g,n} A_{w,w}, \tag{17}$$

where, $q_{w,w}''$ is the heat flux concentrated in the wetting front, $A_{w,w}$ the wetting front area, and $U_{g,n}$ the vapor velocity normal to the wall. Eq. (17) is used to determine $U_{g,n}$. Then, equating the normal vapor momentum, $\rho_g U_{g,n}^2$, to the average pressure difference given by Eq. (16) yields the following relation for the lift-off heat flux concentrated in the wetting front,

$$\begin{aligned} q_{w,w}'' &= \rho_g\left(c_{p,f}\Delta T_{sub,in} + h_{fg}\right)\sqrt{\frac{\overline{p_f - p_g}}{\rho_g}} \\ &= \rho_g\left(c_{p,f}\Delta T_{sub,in} + h_{fg}\right)\left[\frac{4\pi\sigma}{\rho_g}\frac{\sin(b\pi)}{b}\right]^{1/2}\frac{\delta^{1/2}}{\lambda_c}. \end{aligned} \tag{18}$$

4.5. Heated wall energy balance

An energy balance is applied in which the sum of heat dissipated at CHF– in all the wetting fronts is equal to the total heat supplied from the heated wall. The critical heat flux, q_m'', is based on the total wall heat input divided by the total wall area, therefore

$$q_m'' = bq_{w,w}''. \tag{19}$$

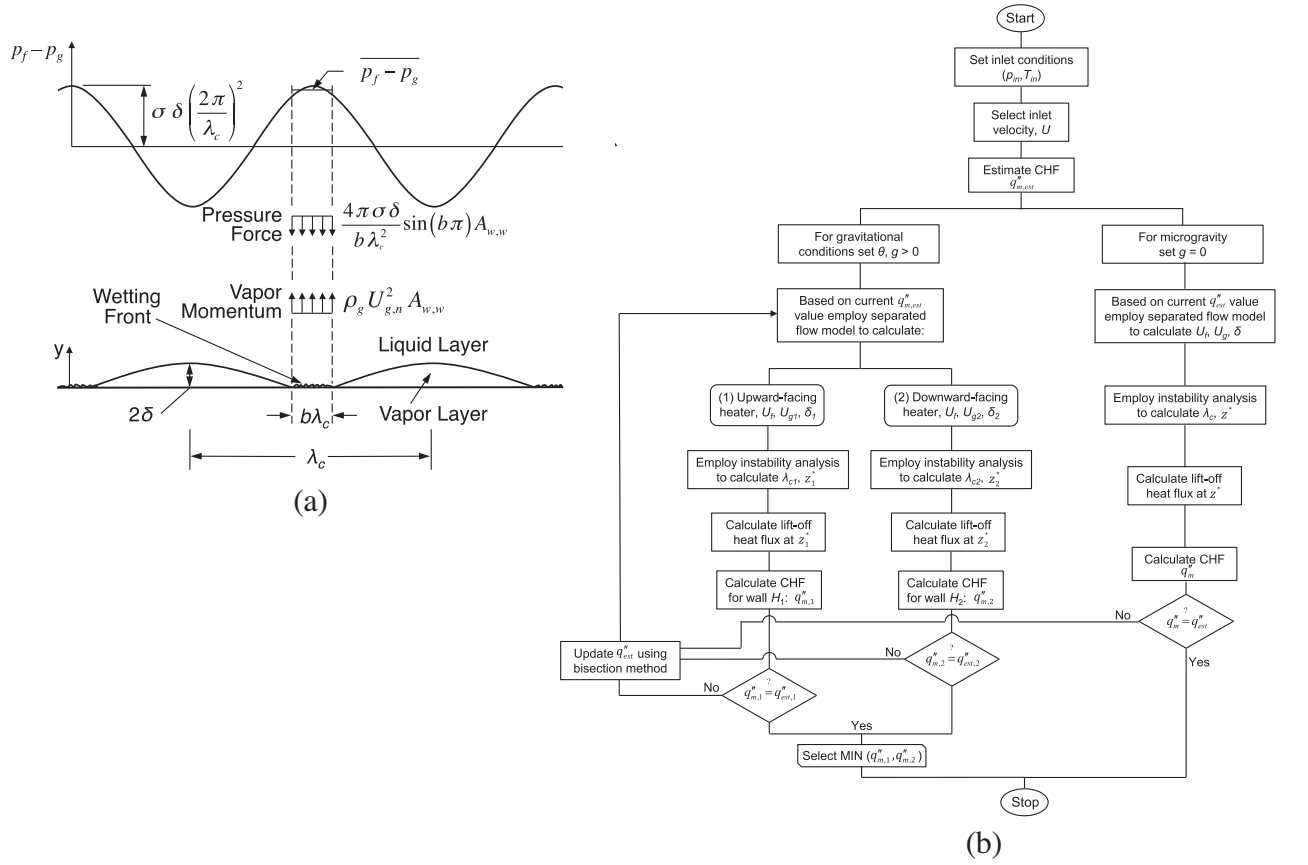

Fig. 10. (a) Schematic representation of Interfacial Lift-off from heated wall in wetting front at CHF. (b) Procedure used to calculate CHF.

Combining Eq. (19) with the expression for heat flux in the wetting front given by Eq. (18) gives the following relation for CHF:

$$q''_m = \rho_g\left(c_{p,f}\Delta T_{sub,in} + h_{fg}\right)\left[\frac{4\pi\sigma b\sin(b\pi)}{\rho_g}\right]^{1/2}\left.\frac{\delta^{1/2}}{\lambda_c}\right|_{z^*}, \tag{20}$$

where the vapor layer thickness, δ, and critical wavelength, λ_c, are calculated at z^*, where the wavy vapor layer is generated.

4.6. CHF model calculation procedure

The CHF model is composed of four major components, and is capable of predicting CHF for subcooled flow boiling in terrestrial and microgravity environments. Combining the different equations associated with the four components requires multiple iterations to arrive at a convergent CHF value. Fig. 10(b) provides a step-by-step procedure for this iterative solution. The procedure is initiated by setting the subcooled inlet conditions at the leading edge of the heaters ($z = 0$) in terms of temperature T_{in}, pressure p_{in}, and inlet flow velocity U. The computations begins with a guessed value for critical heat flux, $q''_{m,est}$, which is used in the separated flow model to determine mean liquid velocity, U_f, as well as mean vapor velocity, U_g, and mean vapor layer thickness, δ, for both heated walls. These parameters are obtained for every z location along the heated length using a fourth-order Runge–Kutta numerical scheme. Next, CHF is determined for subcooled flow boiling in either Earth gravity or microgravity. In Earth's gravity ($g = 1 - g_e$), CHF is influenced by gravitational body force, therefore the Interfacial Lift-off Model will yield different values for upward-facing and downward-facing heated walls, and therefore different CHF values.

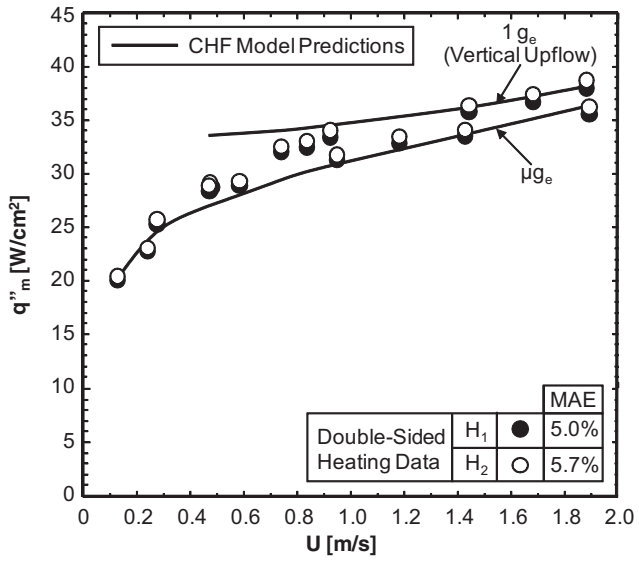

Fig. 11. Comparison of measured and predicted variations of CHF with inlet velocity for double-sided heating in μg_e, along with predicted CHF for double-sided heating in vertical upflow at $1 - g_e$.

In microgravity ($g \approx 0$), body force is negligible, therefore identical CHF values are predicted for both heated walls.

A key step in the iterative solution is to determine z_0, where $U_g = U_f$, using the separated flow model. This is followed by calculating critical wavelength, λ_c, and axial span of the upstream wetting front, z^*, which requires multiple iterations. Using the value of

b = 0.2 recommended in [47,48], CHF is finally determined by evaluating fluid properties, λ_c and δ at z^*. The predicted CHF value, q''_m, is compared with the initial estimate $q''_{m,est}$. If the two values differ by a small pre-specified value, the procedure is terminated, otherwise the entire procedure is repeated using the updated estimate until convergence is achieved.

Notice that, when the model is used to predict CHF for terrestrial conditions, different CHF values will be realized for the two heated walls. The true CHF is chosen as the lowest of the two values. This is based on actual practice in performing flow boiling experiments, where, to avoid any physical damage to the flow channel components, the power to both walls must be simultaneously cut off once CHF is encountered in either wall.

4.7. Comparison of CHF data and model predictions

To explore the effectiveness of the CHF model just presented, the model predictions are compared to the double-sided heating CHF data obtained in μg_e onboard the parabolic aircraft. Fig. 11 shows both the measured and predicted variations of CHF with inlet velocity for double-sided heating in μg_e. Low velocities are shown yielding relatively small CHF values in μg_e, and CHF increases appreciably with increasing flow velocity. Also shown in Fig. 11 are predictions of the CHF model. Both measured and predicted results show CHF increases appreciably with increasing inlet velocity. Moreover, the CHF data are predicted very well in both trend and value. The predictive accuracy of the model is assessed by the mean absolute error defined as

$$MAE = \frac{1}{N}\sum \left| \frac{q''_{m,pred} - q''_{m,exp}}{q''_{m,exp}} \right| \times 100\%, \quad (21)$$

where N is the number of data points. The MAE for the double-sided heating CHF data is 5.0% for H_1 and 5.7% for H_2.

It is important to emphasize that the CHF model is capable of tackling both μg_e and $1-g_e$ conditions. To further investigate CHF trends, predictions for $1-g_e$ vertical upflow with double-sided heating are also presented in Fig. 11. The upflow configuration is unique for $1-g_e$ in that it does not include body force effects normal to the heated walls, which yields equal CHF values for the two walls. Notice how the $1-g_e$ predictions tend to converge with the μg_e data and predictions above $U \sim 1$ m/s. These findings are consistent with single-sided μg_e heating results of Zhang et al. [42], namely: (1) low CHF in low velocity μg_e flow boiling, (2) increasing CHF with increasing velocity, and (3) convergence between μg_e and $1-g_e$ CHF values at high velocities, (4) prevalence of wavy vapor layer and wetting fronts along heated wall at CHF−, and (5) effectiveness of Interfacial Lift-off Model in predicting μg_e flow boiling CHF data. The convergence of CHF data for μg_e and $1-g_e$ around 1 m/s is especially important since knowing the velocity at which convergence occurs allows designers of space systems to achieve inertia-dominated performance as well as to take advantage of prior data and correlations developed from terrestrial studies.

5. Conclusions

In this second part of a two-part study, flow boiling CHF for FC-72 is investigated in microgravity, which was simulated in a series of parabolic flight maneuvers. A rectangular flow channel was used, which was fitted with two opposite heating walls, allowing either one or both walls to be activated during a given test. The main objectives of this part of this study are to capture the trigger mechanism for CHF and develop a mechanistic model for double-sided heating. Key findings from the study are as follows.

(1) CHF− interfacial behavior is consistent with the single-sided heating behavior proposed by Galloway and Mudawar [23,24], where a dominant wavy vapor layer covers the heated walls, with liquid access to the walls sustained only in wetting fronts corresponding to the troughs of the wave. CHF is associated with successive lift-off of wetting fronts from the walls, which is also consistent with the Interfacial Lift-off Model of Galloway and Mudawar.

(2) Data for both single-sided and double-sided heating configurations show CHF increases appreciably with increasing inlet velocity, with double-sided heating providing higher CHF than single-sided for identical inlet conditions and wall heat fluxes. Higher CHF for double-side heating is attributed to formation of two vapor layers compared to one vapor layer for single-sided increasing the velocities of the flow layers more with double-sided heating.

(3) The Interfacial Lift-off Model, which has been validated extensively in past studies using single-sided heating in both μg_e and $1-g_e$, shows remarkable success in predicting μg_e double-sided heating CHF data in both trend and magnitude. Additionally, applying the same model for double-sided heating in vertical upflow at $1-g_e$ points to convergence of CHF values for μg_e and $1-g_e$ for inlet velocities greater than about 1 m/s. Therefore, using velocities above this threshold allows designers of space systems to achieve inertia-dominated performance as well as to adopt prior data and correlations developed from terrestrial studies.

Conflict of interest

None declared.

Acknowledgment

The authors are grateful for the support of this project by the National Aeronautics and Space Administration (NASA) - United States under grant no. NNX13AB01G.

References

[1] F.P. Chiaramonte, J.A. Joshi, Workshop on critical issues in microgravity fluids, transport, and reaction processes in advanced human support technology – final report, NASA TM-2004-212940, 2004.
[2] The National Academies, Recapturing a future for space exploration: life and physical sciences research for a new era, National Academies Press, Washington, DC, 2011.
[3] I. Mudawar, Two-phase micro-channel heat sinks: theory, applications and limitations, J. Electron. Packag. – Trans. ASME 133 (2011) 041002-2.
[4] I. Mudawar, Recent advances in high-flux, two-phase thermal management, J. Therm. Sci. Eng. Appl. – Trans. ASME 5 (2013) 1–15.
[5] T.M. Anderson, I. Mudawar, Microelectronic cooling by enhanced pool boiling of a dielectric fluorocarbon liquid, J. Heat Transfer – Trans. ASME 111 (1989) 752–759.
[6] R.L. Webb, The evolution of enhanced surface geometries for nucleate boiling, Heat Transfer Eng. 2 (1981) 46–69.
[7] D.D. Hall, I. Mudawar, Critical heat flux (CHF) for water flow in tubes. I: Compilation and assessment of world CHF data, Int. J. Heat Mass Transfer 43 (2000) 2573–2604.
[8] D.D. Hall, I. Mudawar, Critical heat flux (CHF) for water flow in tubes. II: Subcooled CHF correlations, Int. J. Heat Mass Transfer 43 (2000) 2605–2640.
[9] H.J. Lee, S.Y. Lee, Heat transfer correlation for boiling flows in small rectangular horizontal channels with low aspect ratios, Int. J. Multiphase Flow 27 (2001) 2043–2062.
[10] L. Lin, R. Ponnappan, Heat transfer characteristics of spray cooling in a closed loop, Int. J. Heat Mass Transfer 46 (2003) 3737–3746.
[11] M. Visaria, I. Mudawar, Theoretical and experimental study of the effects of spray orientation on two-phase spray cooling and critical heat flux, Int. J. Heat Mass Transfer 51 (2008) 2398–2410.
[12] Y. Katto, M. Kunihiro, Study of the mechanism of burn-out in boiling system of high burn-out heat flux, Bull. JSME 16 (1973) 1357–1366.
[13] D.C. Wadsworth, I. Mudawar, Enhancement of single-phase heat transfer and critical heat flux from an ultra-high-flux-source to a rectangular impinging jet of dielectric liquid, J. Heat Transfer – Trans. ASME 114 (1992) 764–768.

[14] M.E. Johns, I. Mudawar, An ultra-high power two-phase jet-impingement avionic clamshell module, J. Electron. Packag. – Trans. ASME 118 (1996) 264–270.
[15] M.K. Sung, I. Mudawar, Experimental and numerical investigation of single-phase heat transfer using a hybrid jet-impingement/micro-channel cooling scheme, Int. J. Heat Mass Transfer 49 (2006) 682–694.
[16] M.K. Sung, I. Mudawar, Correlation of critical heat flux in hybrid jet impingement/micro-channel cooling scheme, Int. J. Heat Mass Transfer 49 (2006) 2663–2672.
[17] T. Oka, Y. Abe, Y.H. Mori, A. Nagashima, Pool boiling of n-Pentane, CFC-113, and water under reduced gravity: parabolic flight experiments with a transparent heater, J. Heat Transfer – Trans. ASME 117 (1995) 408–417.
[18] S.S. Kutateladze, A.I. Leont'ev, Some applications of the asymptotic theory of the turbulent boundary layer, in: Proc. Third Int. Heat Transfer Conf., Chicago, IL, vol. 3, 1966, pp. 1–6.
[19] L.S. Tong, Boundary-layer analysis of the flow boiling crisis, Int. J. Heat Mass Transfer 11 (1968) 1208–1211.
[20] W. Hebel, W. Detavernier, M. Decreton, A contribution to the hydrodynamics of boiling crisis in a forced flow of water, Nucl. Eng. Des. 64 (1981) 443–445.
[21] J. Weisman, B.S. Pei, Prediction of critical heat flux in flow boiling at low qualities, Int. J. Heat Mass Transfer 26 (1983) 1463–1477.
[22] C.H. Lee, I. Mudawar, A mechanistic critical heat flux model for subcooled flow boiling based on local bulk flow conditions, Int. J. Multiphase Flow 14 (1988) 711–728.
[23] J.E. Galloway, I. Mudawar, CHF mechanism in flow boiling from a short heated wall. Part 1: Examination of near-wall conditions with the aid of photomicrography and high-speed video imaging, Int. J. Heat Mass Transfer 36 (1993) 2511–2526.
[24] J.E. Galloway, I. Mudawar, CHF mechanism in flow boiling from a short heated wall. Part 2: Theoretical CHF model, Int. J. Heat Mass Transfer 36 (1993) 2527–2540.
[25] S. Luciani, D. Brutin, C. Le Niliot, O. Rahli, L. Tadrist, Flow boiling in minichannels under normal, hyper-, and microgravity: local heat transfer analysis using inverse methods, J. Heat Transfer – Trans. ASME 130 (2008) 1–13.
[26] S. Luciani, D. Brutin, C. Le Niliot, O. Rahli, Boiling heat transfer in a vertical microchannel: local estimation during flow boiling with a non intrusive method, Multiphase Sci. Technol. 21 (2009) 297–328.
[27] D. Brutin, V.S. Ajaev, L. Tadrist, Pressure drop and void fraction during flow boiling in rectangular minichannels in weightlessness, Appl. Therm. Eng. 51 (2013) 1317–1327.
[28] I. Chen, R. Downing, E.G. Keshock, M. Al-Sharif, Measurements and correlation of two-phase pressure drop under microgravity conditions, J. Thermophys. Heat Transfer 5 (1991) 514–523.
[29] B. Choi, T. Fujii, H. Asano, K. Sugimoto, A study of gas–liquid two-phase flow in a horizontal tube under microgravity, Ann. N.Y. Acad. Sci. 974 (2002) 316–327.
[30] L. Zhao, K.S. Rezkallah, Pressure drop in gas–liquid flow at microgravity conditions, Int. J. Multiphase Flow 21 (1995) 837–849.
[31] M. Misawa, An experimental and analytical investigation of flow boiling heat transfer under microgravity conditions (Ph.D. thesis), University of Florida, 1993.
[32] J. Kim, J.F. Benton, D. Wisniewski, Pool boiling heat transfer on small heaters: effect of gravity and subcooling, Int. J. Heat Mass Transfer 45 (2002) 3919–3932.
[33] T. Oka, Y. Abe, K. Tanaka, Y.H. Mori, A. Nagashima, Observational study of pool boiling under microgravity, JSME Int. J. 35 (1992) 280–286.
[34] J.F. Zhao, J. Li, N. Yan, S.F. Wang, Bubble behavior and heat transfer in quasi-steady pool boiling in microgravity, Microgravity Sci. Technol. 21 (2009) 175–183.
[35] H. Ohta, Experiments on microgravity boiling heat transfer by using transparent heaters, Nucl. Eng. Des. 175 (1997) 167–180.
[36] Y. Ma, J.N. Chung, An experimental study of critical heat flux (CHF) in microgravity forced-convection boiling, Int. J. Multiphase Flow 27 (2001) 1753–1767.
[37] H. Zhang, I. Mudawar, M.M. Hasan, Experimental assessment of the effects of body force, surface tension force, and inertia on flow boiling CHF, Int. J. Heat Mass Transfer 45 (2002) 4079–4095.
[38] H. Zhang, I. Mudawar, M.M. Hasan, Experimental and theoretical study of orientation effects on flow boiling CHF, Int. J. Heat Mass Transfer 45 (2002) 4463–4478.
[39] H. Zhang, I. Mudawar, M.M. Hasan, A method for assessing the importance of body force on flow boiling CHF, J. Heat Transfer – Trans. ASME 126 (2004) 161–168.
[40] H. Zhang, I. Mudawar, M.M. Hasan, Investigation of interfacial behavior during the flow boiling CHF transient, Int. J. Heat Mass Transfer 47 (2004) 1275–1288.
[41] H. Zhang, I. Mudawar, M.M. Hasan, Photographic study of high-flux subcooled flow boiling and critical heat flux, Int. Commun. Heat Mass Transfer 34 (2007) 653–660.
[42] H. Zhang, I. Mudawar, M.M. Hasan, Flow boiling CHF in microgravity, Int. J. Heat Mass Transfer 48 (2005) 3107–3118.
[43] H. Zhang, I. Mudawar, M.M. Hasan, CHF model for subcooled flow boiling in Earth gravity and microgravity, Int. J. Heat Mass Transfer 50 (2007) 4039–4051.
[44] C. Konishi, H. Lee, I. Mudawar, M.M. Hasan, H.K. Nahra, N.R. Hall, J.D. Wagner, R.L. May, J.R. Mackey, Flow boiling in microgravity: Part 1 - Interfacial behavior and experimental heat transfer results, Int. J. Heat Mass Transfer 81 (2015) 705–720.
[45] C.O. Gersey, I. Mudawar, Effects of heater length and orientation on the trigger mechanism for near-saturated flow boiling critical heat flux. I: Photographic study and statistical characterization of the near-wall interfacial features, Int. J. Heat Mass Transfer 38 (1995) 629–641.
[46] C.O. Gersey, I. Mudawar, Effects of heater length and orientation on the trigger mechanism for near-saturated flow boiling critical heat flux. II: Critical heat flux model, Int. J. Heat Mass Transfer 38 (1995) 643–654.
[47] J.C. Sturgis, I. Mudawar, Critical heat flux in a long, rectangular channel subjected to onesided heating. I: Flow visualization, Int. J. Heat Mass Transfer 42 (1999) 1835–1847.
[48] J.C. Sturgis, I. Mudawar, Critical heat flux in a long, rectangular channel subjected to onesided heating. II: Analysis of critical heat flux data, Int. J. Heat Mass Transfer 42 (1999) 1849–1862.
[49] C.R. Kharangate, I. Mudawar, M.H. Hasan, Experimental and theoretical study of critical heat flux in vertical upflow with inlet vapor void, Int. J. Heat Mass Transfer 55 (2012) 360–374.
[50] C.R. Kharangate, I. Mudawar, M.H. Hasan, Photographic study and modeling of critical heat flux in horizontal flow boiling with inlet vapor void, Int. J. Heat Mass Transfer 55 (2012) 4154–4168.
[51] C. Konishi, I. Mudawar, M.M. Hasan, Investigation of the influence of orientation on critical heat flux for flow boiling with two-phase inlet, Int. J. Heat Mass Transfer 61 (2013) 176–190.
[52] C. Konishi, I. Mudawar, M.M. Hasan, Criteria for negating the influence of gravity on flow boiling critical heat flux with two-phase inlet conditions, Int. J. Heat Mass Transfer 65 (2013) 203–218.
[53] C. Konishi, I. Mudawar, M.M. Hasan, Investigation of localized dryout versus CHF in saturated flow boiling, Int. J. Heat Mass Transfer 67 (2013) 131–146.
[54] M.S. Bhatti, R.K. Shah, Turbulent and transitional convective heat transfer in ducts, in: S. Kakac, R.K. Shah, W. Aung (Eds.), Handbook of Single-Phase Convective Heat Transfer, John Wiley and Sons, New York, 1987.
[55] H. Lamb, Hydrodynamics, sixth ed., Dover Publications, New York, 1945.
[56] L.M. Milne-Thompson, Theoretical Hydrodynamics, fourth ed., Macmillan, New York, 1960.